Energy dependences of absorption in beryllium windows and argon gas

C. T. Chantler[a] and J.-L. Staudenmann
National Institute of Standards and Technology, Quantum Metrology Division, Building 221, Room A141, Gaithersburg, Maryland 20899

(Presented on 19 July 1994)

In part of an ongoing work on x-ray form factors, new absorption coefficients are being evaluated for all elements, across the energy range from below 100 eV to above 100 keV. These new coefficients are applied herein to typical problems in synchrotron radiation stations, namely the use of beryllium windows and argon gas detectors. Results are compared with those of other authors. The electron–ion pair production process in ionization chambers is discussed, and the effects of $3d$-element impurities are indicated. © *1995 American Institute of Physics.*

I. INTRODUCTION

Synchrotron studies typically use corrections for window absorption, detector efficiency, crystal reflection properties, and other details in order to extract absolute measurements of desired quantities. Some of these have been conveniently found in tables of attenuation coefficients or in programs designed for specific beamlines and compiled from various sources. Often the database used is inappropriate in some significant respect, and it is not uncommon that observed experimental behavior does not tally closely with the theoretical prediction derived from such compilations.

In part of an ongoing work on the x-ray form factors,[1,2] new absorption coefficients are being tabulated for all elements, over the energy range from below 100 eV to above 100 keV. These new coefficients have been compared with those of other authors.[3–6] This paper intends to demonstrate the type and magnitude of effects which are likely to appear in beamline arrangements. Several common difficulties and features of typical spectra will be discussed. Figure 1 shows experimental data taken at the National Synchrotron Light Source X4A beamline[7] in the first ion chamber, 23 m from the source and separated from the source by a double flat Si 111 crystal monochromator, three Be windows of 0.127 mm thickness each, four Kaptan windows of 0.0254 mm thickness, and a small air gap. The active length of the argon-filled ion chamber was $L=33.5\pm0.5$ mm. These experimental parameters were used in the preliminary and subsequent modeling.[8]

The energies selected by the Kohzu KMA-15 monochromator[9] were stepped in uneven intervals and cycled as qualitatively implied by the data. Five independent sets of x-ray flux were measured as a function of beam energy and normalized to a ring current of 200 mA. This addressed time-dependent and other drifts of the beam and instrument. It can be seen that the raw scatter is large and displays a training effect for each day, so that "Data 4" and "Data 3" cycles show improved alignment optimization (and hence reflectivities) than the first cycles. At some level, this indicates a limitation regarding absolute measurements. Optimum alignment corresponds to a profile through the maximum values of the data points.

It is also clear that useful conclusions can be drawn regarding the origin of certain discrepancies from computed fluxes. Initial computations were performed using a modeling program.[8] There is an observable discrepancy at high energies, another at low energies, and a flattening at intermediate energies compared to standard modeling. The simple model used transforms the synchrotron flux F in standard units (photons /s/mA/0.1% bandwidth/horizontal mrad) to the current and voltage delivered by the detector. This has made use of an energy bandpass for Si 111 double-crystal diffraction of $\delta E=10\%$ of the "0.1% bandwidth" or $\delta E/E=0.01\%$; a collimating slit of horizontal aperture $h=0.609$ mrad and vertical aperture 2.0 mm; the current normalization to $I=200$ mA; and a current amplifier amplification factor of $A=10^7$ V/A. As with the experimental data, significant uncertainties arise from the beam distribution and related assumptions. The beam has an estimated vertical full width at half-maximum of 2.3 mm, yielding an estimated attenuation of $v=0.7$ for this contribution. Then

$$V=A_P I A h v\,\delta E e I_P, \tag{1}$$

$$A_P=F[1-\exp(-\mu_{PE}\rho L)], \tag{2}$$

$$I_P=E/\epsilon, \tag{3}$$

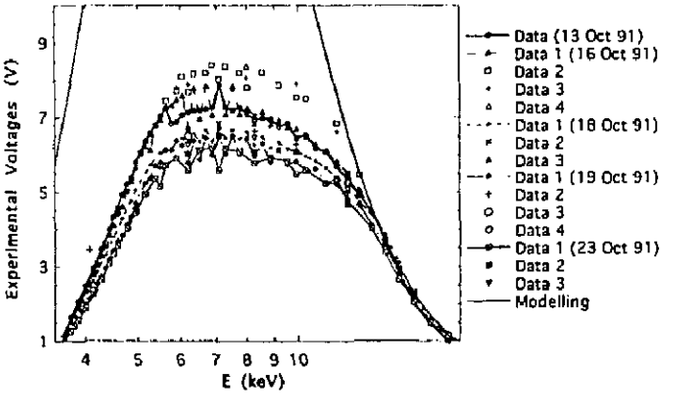

FIG. 1. *Comparison of simple model with complete set of data, as experimental voltages, for NSLS beamline X4A and first ion chamber. Note the training effect and variation of data and large discrepancy of model below 10 keV.*

[a]Present address: School of Physics, University of Melbourne, Parksville, Vic. 3052, Australia.

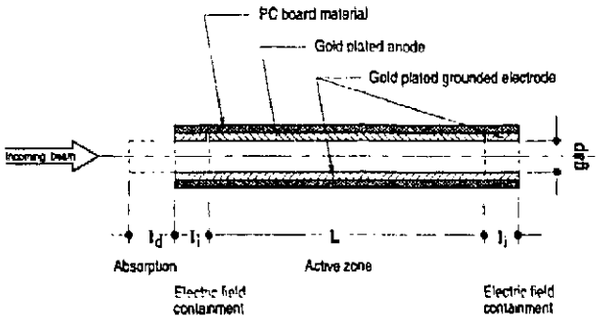

FIG. 2. Profile of ion chamber detector geometry, indicating ion-pair production regions: absorption, intermediate, and active zones. The grounded part on the anode board surrounds the active area, as indicated by the electric field containment.

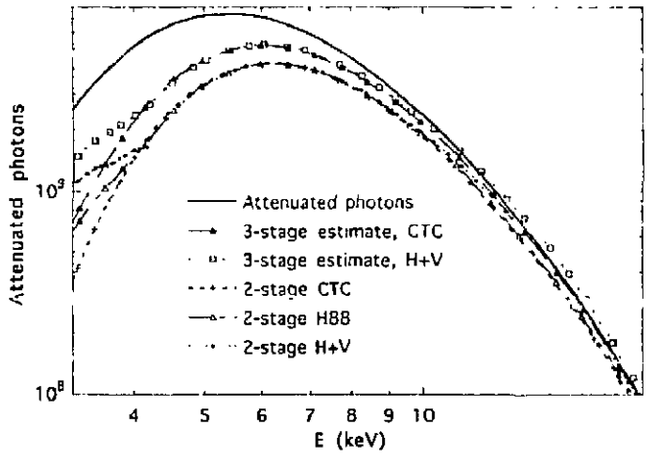

FIG. 3. Models for argon recombination in the ion chamber. The solid line is the simple model for attenuated photons: the three-stage model is expected to be a more reasonable estimate, while the two-stage model should overestimate recombination, or lead to fewer effective primary attenuated photons. CTC uses coefficients following Refs. 1 and 2; H88 uses coefficients from Refs. 3 and 4; H+V includes scattering cross sections from Ref. 5. Variation between extremes and different attenuation models is large.

where $e=1.602\times10^{-19}$ J and the photon energy E is given in the same units as ϵ, to provide I_P, the number of ion pairs per attenuated photon, for the number of attenuated photons A_P.

The model assumes an ideal, complete argon gas conversion to ion pairs for attenuated photons, with a mean energy per ion pair of $\epsilon=27.2\pm1.8$ eV. This is derived in an *ad hoc* manner from the average of references in Ref. 10. There is expected to be an energy dependence for these measurements, or at least a distribution of systematic corrections, which to first order is contained within the above standard deviation. This average may be contrasted with a reported range of ϵ from 24.4 to 30.0 eV, or M-edge binding energies[1–4] (which serve as a lower estimate) from 15.7 to 29.3 eV.

II. LOW ENERGY CORRECTION (ARGON GAS)

The largest discrepancy of the theoretical result from experiment is at the lowest energies. This is due primarily to the detector characteristics and argon attenuation prior to the active region. While simple in principle, this correction is complicated by the geometry and the interrelation between field strengths and recombination rates at the lower edge of the ion chamber I/V plateau region. This region prior to the active region is 8 ± 1 mm in the relevant chamber, with a 1 atm (+1%) flow of pure argon gas.

The naive model of Eq. (2) assumed that this prior region was nonexistent; whereas a simple underestimate of the conversion efficiency in a two-stage model would assume that it was purely attenuating, with a 15% correction[11–13] for recombination within the 300 V ion chamber potential across the 10 mm gap in the 33.5 mm×28.0 mm parallel-plate ion chamber (Fig. 2). A more accurate simple treatment would divide the ion chamber into three regions: a dead layer ($l_d=4$ mm) where attenuation dominates and no ion-pairs propagate; an active region (of 33.5 mm) where photoelectric absorption yields the expected ion pairs with an estimated average recombination loss of 8%; and an intermediate region ($l_i=4$ mm) where recombination occurs for 50% of the total events. Hence Eq. (2) is replaced by

$$A_P=F\exp(-\mu_{PE}\rho l_d)\{[1-\exp(-\mu_{PE}\rho l_i)]P_1 + \exp(-\mu_{PE}\rho l_i)[1-\exp(-\mu_{PE}\rho L)]P_2\}, \quad (4)$$

$$P_1=0.50, \quad P_2=0.92, \quad \rho=0.0017837 \text{ g cm}^{-3}. \quad (5)$$

Use of total attenuation coefficients or different photoelectric absorption coefficients has a large effect near the K edge, as illustrated in Fig. 3. The three-stage model using coefficients for photoelectric absorption in the last two regions, with data following Chantler,[1,2] is expected to be more accurate than other models. However the comparison indicates both possible errors from certain assumptions, and plausible uncertainties in different energy ranges. Using logarithmic scales suppresses details at high or low energies, but conveys the overall pattern more clearly.

III. LOW–MEDIUM ENERGY CORRECTION (ION-PAIR PRODUCTION)

Considering that the three-stage model for recombination is adequate, but treating the two-stage model as an indication of uncertainty and possible error, the result may be compared to experimental voltages using Eqs. (1) and (3)–(5). However, the models still overestimate the data. All argon L- and M-shell attenuation transfers energy via Auger processes to yield low-energy photoelectrons, which produce the cascade to low-energy ion pairs of mean energy ϵ. However, some of the absorbed K-shell photons are re-emitted in fluorescence. This fluorescence yield (mainly $K\alpha$ radiation) can escape from the ion chamber without further ion-pair conversion; or it may be photoabsorbed hy a second argon atom. A second correction is therefore necessary, arising from the ion-pair production process inside the ion chamber, replacing Eq. (3) by Eq. (6):

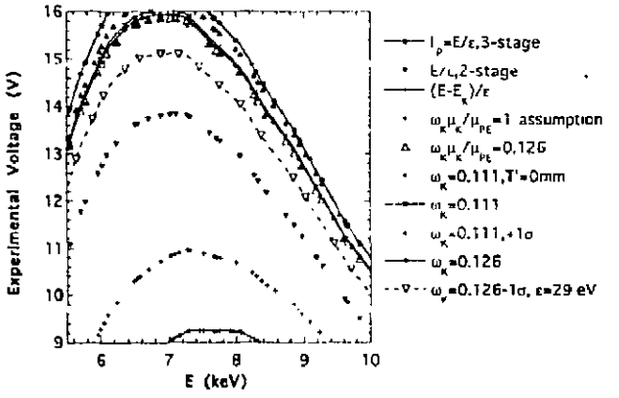

FIG. 4. Models for ion-pair formation in the detector, leading to predictions for experimental voltages. Models and variation as discussed in the text.

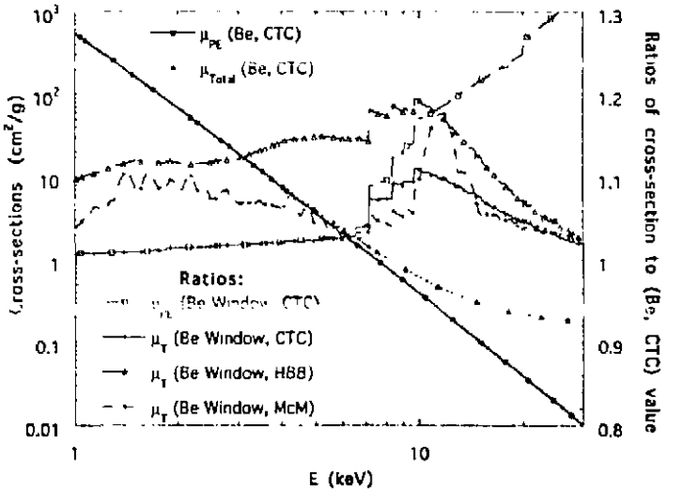

FIG. 5. Variation of attenuation coefficients for beryllium and beryllium windows with energy, and with different attenuation coefficients. CTC follows Refs. 1 and 2; H88 uses Refs. 3–5; and McM uses Ref. 6. Other details are described in the text.

$$I_P=[E-\omega_K(\mu_{EK}/\mu_{PE}) \times\{E_K+E_{K\alpha}[1-\exp(-\mu_{PE\alpha}\rho T')]\}]/\epsilon. \quad (6)$$

Here $E_K=3.2029$ keV is the K-edge energy,[1–4] $E_{K\alpha}=2.9577$ keV is the $K\alpha$ energy,[1–4] $\mu_{PE\alpha}$ is here specific for this latter energy, $T'=10\pm3$ mm is a mean distance to the chamber edge, ω_K is the fluorescence yield (relative to Auger processes), and (μ_{EK}/μ_{PE}) indicates the ratio of photoabsorption due to the K shell compared to the total, is energy dependent, and is typically of order 0.9 in the region above 3.5 keV. Various simpler estimates follow setting the energy-dependent $(\mu_{EK}/\mu_{PE})=1$ (neglecting L- and M-shell absorption above the K edge), or setting $T'=0$ mm (neglecting secondary photoabsorption).

Figure 4 indicates the magnitude of these contributions for a narrow energy range, noting that the dependences on energy vary significantly. Equation (3) is much more appropriate than use of $I_P=(E-E_K)/\epsilon$ or $[E-\{E_K+E_{K\alpha}[1-\exp(-\mu_{PE}\rho T')]\}]/\epsilon$ [or equivalently $\omega_K(\mu_{EK}/\mu_{PE})=1$], which correspond to the neglect of fluorescence yields and/or secondary absorption. These three formulas give the largest values and the minimum two plots for all energies, as indicated in the Fig. 4. The two-stage model indicates the effect of differing recombination on the final experimental voltage, and hence limiting uncertainty from this source.

Open triangles represent the simplest realistic estimate, using an accurate fluorescence yield[14] but assuming that all absorption is due to the K shell; which is seen to be almost equivalent to the use of a low but published fluorescence yield,[15] combined with neglect of secondary absorption (small filled squares in Fig. 4). Combining all these effects with a low fluorescence yield $\omega_K=0.111$ provides one of the best estimates, while use of $\omega_K=0.126$ provides another. For most of this energy range, these two alternatives are similar. Upper uncertainty limits are given by closed triangles, while lower uncertainty limits are given by open inverted triangles. Uncertainties due to recombination at the 20% level are indicated by the two-stage model, while 10% uncertainties from ω, secondary absorption length T', and ϵ are indicated in the plot. Not plotted are significant variations from use of other photoabsorption or attenuation estimates,[3–6] which tend to raise the expected voltage by up to 10% in this region (and more elsewhere).

IV. LOW–MEDIUM ENERGY CORRECTION (BERYLLIUM WINDOWS)

The beamline attenuation from beryllium windows assumes in general that pure beryllium is appropriate and that the old attenuation coefficients[6] are adequate. At sufficiently high energies this is quite acceptable, since scattering dominates and the windows become optically thin. Every window from reputable suppliers comes with a chemical analysis indicating purity of typically 99.92% with significant oxide, carbon, iron, nickel, silicon, and zinc contamination, together with traces of such elements as aluminum, copper, silver, and lead. One consequence of this is that the mean density of the window is about 0.2% higher than that of pure beryllium.

Much more significant is the influence of (mainly K-shell) edges of these impurities. In estimating this effect, we have used an average of data from three foils, which may be considered as typical. The exponential range of attenuation cross section with energy is such that significant differences are poorly discerned; Fig. 5 displays the photoelectric and total cross sections for pure beryllium with current coefficients.[1,2] Scattering becomes significant around 6–8 keV as the difference between the curves for photoelectric cross sections (open circles) and total cross sections (filled triangles).

Compared to the photoelectric coefficient for pure beryllium, that for beryllium windows is similar below 4 keV but shows large corrections above the major edges, reaching a 35% correction at 30 keV. The ratio of total attenuation of the window compared to pure Be peaks at 12%, at around 10 keV, and declines thereafter as the scattering processes begin to dominate.

Coeficients from Ref. 6 are plotted in Fig. 5, normalized by the values following Refs. 1 and 2. Corrections of 10% in

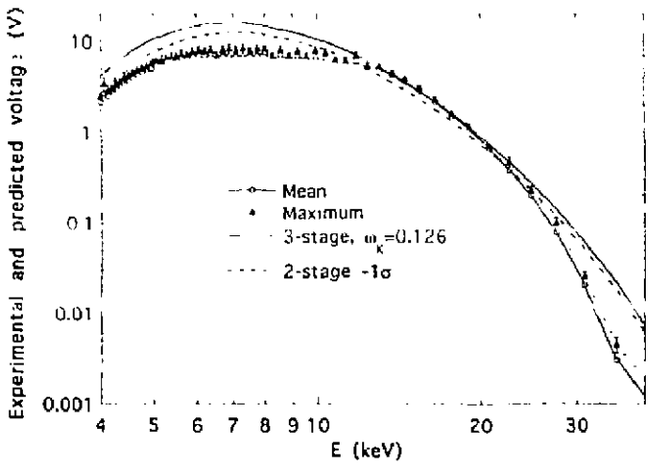

FIG. 6. The top curve is the predicted three-stage voltage, corrected for effects in the text. The two-stage model, below, is an estimate of modeling uncertainty, lying above the experimental estimate based on maxima, and the lowest curve of experimental averages.

the 1–3 keV region and in the 8–15 keV region indicate significant imprecision of the early result. Comparison to Refs. 3–5 also reveal 10%–20% discrepancies in this 1–15 keV range. These significant differences clearly have a major effect on attenuation at lower energies.

V. HIGH ENERGY BEHAVIOR (MONOCHROMATOR ALIGNMENT)

Figure 6 shows the overall agreement of the corrected estimate compared to the average and maximum data sets, with imprecision of the estimate indicated by the two-stage model and error bars on the data given by the standard deviation of the data. From 12 to 20 keV, the data and experiment are in good agreement. Above 22 keV, a high energy discrepancy is observed, which may be understood as a misalignment of the monochromator crystals with the ion chamber entrance slit, of approximately 1 mm (the crystals are truncated diamonds 60 mm×150 mm).

VI. LOW–MEDIUM ENERGY DIP (RECOMBINATION)

At low energies there is a significant discrepancy due to scaling errors or inadequacies of flux (alignment) optimization. However, there is an observable dip between 5 and 12 keV compared to the above estimates, arising from two sources.

The monochromator diffraction width was taken as $\Delta E/E = 10^{-4}$ which is a relatively poor estimate. This neglects a dependence upon Bragg angle and polarization effects. Hence the efficiency will decrease at low energies, or the low end of the experimental data region.

Our computation of recombination was a simple approximate model. Where the synchrotron flux is greatest (in this energy region), the available number of ion pairs per volume is greater and the percentage of pairs recombining increases significantly. In addition, at lower energies the dominant conversion to electron–ion pairs occurs in shorter and shorter length of the active region of the detector, so that actual ion-pair production is further concentrated (compared to the high energy or low flux regions). The simple models discussed neglect this type of detail, which would indeed produce a dip and a flattening of the peak voltage.

VII. CONCLUSIONS

Agreement of experiment and theory for synchrotron beamlines can be substantially improved by consideration of ion-pair recombination, inactive and intermediate detector regions, fluorescence and secondary photon attenuation, beryllium window impurities, and improved attenuation cross sections. Overall agreement with relatively simple assumptions was improved in the current context from order of magnitude errors to a factor of 2 discrepancy in the regions of poorer agreement. This agreement is partially commensurate with contributing uncertainties of model parameters. Differences between cross-section tabulations and formalisms can be quite significant. This paper indicates further modeling to be pursued to improve the comparison of theory and experiment further. It may be noted however, that current agreement is substantially improved compared to earlier comparisons of modeling and experiment.[8]

ACKNOWLEDGMENT

The authors wish to acknowledge the assistance of L. D. Chapman with the synchrotron modeling program.

[1] C. T. Chantler, Rad. Phys. Chem. **41**, 759 (1993).
[2] C. T. Chantler, in *X-ray Resonance (Anomalous) Scattering*, edited by G. Materlik, K. Fischer, and C. J. Sparks (Elsevier, Amsterdam, in press).
[3] B. L. Henke, J. C. Davis, E. C. Gullikson, and R. C. Perera, Lawrence Berkeley Laboratory Report No. LBL-26259 UC-411, 1988.
[4] B. L. Henke, E. C. Gullikson, and J. C. Davis, At. Data Nucl. Data Tables **54**, 181 (1993); **55**, 349(E) (1993).
[5] W. J. Veigele, At. Data Nucl. Data Tables **5**, 51 (1973).
[6] W. H. McMaster, N. Kerr del Grande, J. H. Mallett, and J. H. Hubbell, University of California Laboratory Report No. UCRL-50174, 1967.
[7] J.-L. Staudenmann, W. A. Hendrickson, and R. Abramowitz, Rev. Sci. Instrum. **60**, 1939 (1989).
[8] D. Chapman, N. Gmur, N. Lazarz, and W. Thomlinson, Nucl. Instrum. Methods A **266**, 191 (1988); for experimental comparison, E. Brauer and W. Thomlinson, *ibid.* **266**, 195 (1988).
[9] A. Koyama, M. Nomura, H. Kawata, T. Iwazumi, M. Sato, and T. Matsushita, Rev. Sci. Instrum. **63**, 916–919 (1992); T. Matsushita, T. Ishikawa, and H. Oyanagi, Nucl. Instrum. Methods A **246**, 377 (1986). This identification does not imply endorsement nor should it be taken to suggest that the identified items are necessarily best suited for the applications in which they are used.
[10] U. W. Arndt and B. T. M. Willis, *Single Crystal Diffractometry* (Cambridge University Press, Cambridge, 1966); L. V. Azaroff, *Elements of X-ray Crystallography* (McGraw-Hill, New York, 1968); J.-P. Eberhart, *Méthode Physiques d'Etude des Minéraux et des Matériaux Solides* (Doin Editeurs, Paris, 1976); J. M. Valentine, Proc. R. Soc. London, Ser. A **211**, 75 (1952); J. Weiss and W. Bernstein, Phys. Rev. **98**, 1828 (1955); O. Gaertner, Ann. Phys. **10**, 825 (1931); **2**, 94 (1929); J. G. Timothy and R. P. Madden, *Photon Detectors for the Ultraviolet and X-ray Region, Handbook on Synchrotron Radiation*, edited by G. F. Koch (North-Holland, Amsterdam, 1983), Vol. 1A; G. F. Knoll, *Radiation Detection and Measurement* (Wiley, New York, 1979).
[11] G. F. Knoll, *Radiation Detection and Measurement* (Wiley, New York, 1979), p. 159.
[12] C. A. Colmenares, Nucl. Instrum. Methods **114**, 269 (1974).
[13] H. E. Johns and J. R. Cunningham, *The Physics of Radiology*, 4th ed. (Thomas, Springfield, IL, 1983), p. 290.
[14] E. J. McGuire, Phys. Rev. A **2**, 273 (1970).
[15] V. O. Kostroun, M. H. Chen, and B. Crasemann, Phys. Rev. A **3**, 533 (1971).